Shear-Band Dynamics in Metallic Glasses

Robert Maaß and Jörg F. Löffler**

The future of metallic glasses as an advanced structural and functional material will to a great extent depend on the understanding and control of their mesoscopic flow defects called shear bands. These defects are sweet-and-sour; sweet because they mediate macroscopic plasticity at room temperature, and sour because they quickly promote failure. In the past decade, fundamental research generated great progress in characterizing the role that shear bands play during plastic deformation of disordered systems, including metallic glasses. Similar to those in many other materials, shear bands in metallic glasses are only active for a very short time, which directed research focus towards topological, structural, chemical, and thermal properties of formed, but inactive shear bands. In this paper, recent progress in directly characterizing the shear-band dynamics in situ during straining experiments is presented. Various shear-banding stages are outlined, including formation, propagation, and arrest, as well as shear-band creep and aging. The results are discussed in a more general context of disordered materials, concluding with a summarizing overview of time-scales involved in shear banding, and describing future research directions that may lead to controlled shear-band plasticity in metallic glasses.

1. Introduction

Shear bands are not unique to metallic glasses (MGs), but form in a variety of materials that are put under stress. Examples are fluids, granular solids, polymers, and also crystalline metals. A shear band arises due to localization of strain, where a restricted volume of the material shears relative to the rest. An important aspect is that the sheared volume develops as a layer in the material that remains narrow in the dimension orthogonal to the shearing layer, but can transect the entire sample volume along any in-plane dimension of the layer. As a result, the shearing region looks like a band on the surface of the sample; thus the terminology shear band. Due to the shear band's spatial restriction in one dimension, plastic strain of the entire sample is rather small, but the local shear strain of the deforming material is very high (≈100 in a MG for one single shear event, and up to 10 000 for a few percent of plastic strain). Whereas many materials share shear-band mediated plasticity, the origin and process can be different: in granular media shear-banding initiates due to local density fluctuations and packing imperfections;[1] in crystalline metals shear bands can be formed due to geometric softening where a large group of grains quickly form a texture that is favorably oriented for shear;[2] in time-dependent complex fluids a shear band is created when different viscosities co-exist as a result of an imposed shear-rate;[3] and in amorphous polymers shear bands develop via chain alignment processes leading to shear-thinning.[4] The highly localized and fast deformation via shear-banding is combined with a shear-softening of the involved material. Therefore it is often autocatalytic and detrimental, if compared to deformation that is distributed throughout the entire volume of the material. Metallic glasses themselves demonstrate this when one compares elongation at failure at room temperature (i.e., far below the glass transition) with high-temperature plasticity, where MGs deform homogenously. The ductility-limiting nature of shear bands has provoked tremendous research efforts to understand shear-band formation and shear-band dynamics, but because of the spatial and temporal confinements they are experimentally difficult to study. As in any other material that exhibits shear banding, the spatio-temporal localization is amplified by the intermittent activation at unpredictable locations. As a result, the majority of investigations have concentrated on inactive, already formed shear bands, and only lately dynamic properties of shear bands in metallic glasses have been subject of experimental efforts—a direction that we believe will provide answers to long-standing questions of plasticity in amorphous metals, and that will identify tunable parameters that control shear-band plasticity.

Dr. R. Maaß
Institute for Materials Physics
Georg-August University Göttingen
Friedrich-Hund Platz 1, 37077 Göttingen, Germany
E-mail: robert.maass@ingenieur.de
Prof. J. F. Löffler
Laboratory of Metal Physics and Technology
Department of Materials
ETH Zurich
Vladimir-Prelog-Weg 4, 8093 Zurich, Switzerland
E-mail: joerg.loeffler@mat.ethz.ch

DOI: 10.1002/adfm.201404223

2. Overview on Mechanical Behavior of Metallic Glasses

The mechanical performance and underlying deformation mechanisms of MGs have been summarized extensively in various reports,[5–8] why we will limit ourselves to selected aspects relevant to this feature article. Due to their disordered structure with only short- and medium-range order, lattice defects as known for crystalline metals are undefined in MGs.

Instead, fluctuations in the atomic topology and chemistry allow local plastic transformations. At those sites a single or several atoms may reorganize under an applied stress and temperature. From that perspective plasticity is thermally activated, as in crystalline metals, with the significant difference that a local structural transition in a MG must be regarded as a transient state, which cannot be identified at the atomic scale after its occurrence. In crystals, however, dislocation mechanisms and structural damage can be traced directly as disturbances in the long-range order. Furthermore, in contrast to crystalline materials, MGs do not exhibit strain hardening, which indicates that the interactions of regions undergoing local structural transitions do not strengthen the material. Whereas the details of atomic-scale deformation are still a topic of intense research and primarily looked upon with simulations, the first concepts that explained and modeled deformation of MGs are: i) the "free volume" model by Spaepen,[9] who developed the original description by Turnbull and Cohen[10] further to apply it to MGs, and ii) the "shear-transformation" model by Argon and co-workers.[11,12] The first one essentially views the disordered glassy structure as fluctuations of local volume, and at sites with higher free volume single atomic jumps have a lower energy barrier to overcome. The free-volume model is therefore similar to a diffusion problem with a characteristic activation energy of about 1–2 eV. A shear-transformation (ST, and increasingly common "shear-transformation zone", STZ, after the introduction by Falk and Langer)[13] involves a number of atoms (a few to ≈100) and has a characteristic activation energy range that is at the low end similar to that of the free-volume model, but can also reach values of up to about 5 eV. At the atomic scale these two classical viewpoints by Spaepen and Argon appear fundamentally different, but they also share many similarities. Both are thermally activated and describe a process that is dilatational upon overcoming its transition barrier. Structural transitions can go forward and backward, redistribute local stress and strain, and allow the accumulation of local excess free volume, which is believed to play a crucial role in the formation of mesoscopic flow defects; that is shear bands.

More recent frameworks on STZ dynamics are an extension of these two classical descriptions, but additionally include orientational degrees of freedom and an effective disorder temperature.[13–15] In particular the latter one, which describes the amount of configurational disorder in the material, has enabled a successful description of strain localization and the formation of shear bands,[16,17] and also generated a base for the development of a continuum elastoplastic STZ theory that is capable of modeling necking instabilities.[18] Despite the successes of recent STZ theory to describe deformation in disordered systems, one has to keep in mind that it relies on athermal structural transitions with a density of STZs that is quite low.[19] In order to describe the dynamics of shear-banding, Daub et al. have thus extended recent STZ theory by introducing a thermally activated relaxation term.[20] With this extension it is possible to quantitatively describe various dynamic shear-banding phenomena, such as aging dynamics and stick-slip shear-banding, which are outlined in this manuscript. Furthermore, one has to keep in mind that the disordered structure should contain a very high number of possible structural transitions.

Robert Maaß obtained a diploma in materials science and engineering from the Institut National Polytechnique de Lorraine (EEIGM), Luleå Technical University and Saarland University in 2005. Subsequently, he developed an in situ Laue microdiffraction setup to study size-affected plasticity at the Swiss Light Source and received his PhD in 2009 from the EPFL in Lausanne. From 2009–2011 he was a postdoctoral researcher at ETH Zurich investigating deformation behavior of metallic glasses. During his Alexander von Humboldt scholarship at Caltech he continued his research on plasticity of both small scale crystals and metallic glasses. After being a junior research group leader at the University of Göttingen in Germany, he was appointed assistant professor at the University of Illinois at Urbana-Champaign.

Jörg F. Löffler studied physics and materials science at Saarland University, Germany, and obtained his doctorate at the Paul Scherrer Institute and ETH Zurich in nano-magnetism and neutron scattering (1997). Löffler then performed research at Caltech, Pasadena, in the area of bulk metallic glasses and was subsequently appointed Assistant Professor at the University of California, Davis (2001). He then became Assistant Professor (2003) and Full Professor (2007) at ETH Zurich, where he chaired the Department of Materials from 2010–2013. Löffler's current research interests lie in the areas of nanostructured and amorphous materials; magnetic, structural, and mechanical properties on the nanoscale; bioresorbable implants; and neutron scattering and synchrotron radiation.

This consequently implies a broad distribution of both activation energies and related structural configurations that puts (extreme value) statistics during thermally activated plasticity below the glass transition into focus.[21–23] Various reports using the so called activation-relaxation technique (ART)[24] to explore the potential energy landscape and potential transition pathways have recently provided detailed insights into the atomistic deformation mechanisms and how they may lead to macroscopic plastic flow.[25–28]

At the macroscopic scale, the deformation behavior of MGs can be summarized in a deformation map with essentially

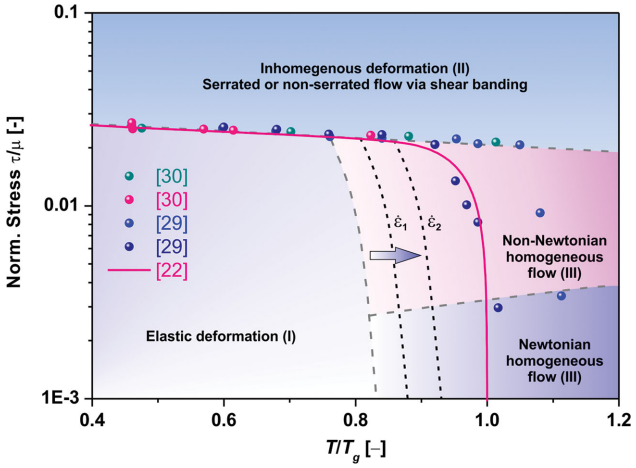

Figure 1. Normalized shear stress as a function of normalized temperature, containing different deformation regimes for MGs; adapted from the literature.[5] The dashed lines are schematic boundaries that have parameter-dependent locations. All data points are experimental data taken from Refs. [29,30] for different MGs tested at different strain rates, and the full line is given by a recent thermal activation model.[22]

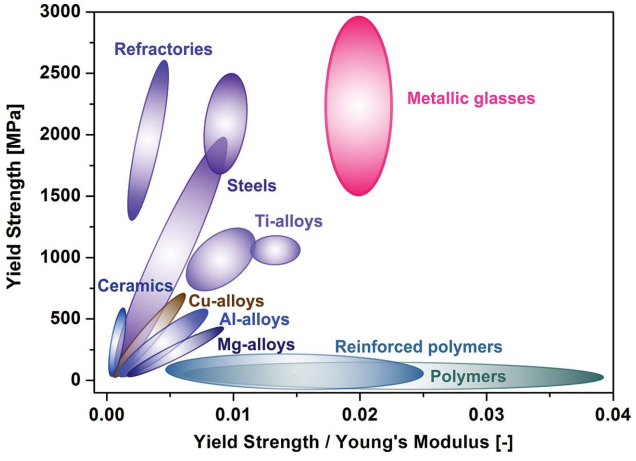

Figure 2. Strength-elasticity correlation for different groups of structural materials. MGs are clearly located at the highest combined values in comparison to all other materials. The general domains for the different materials classes were approximated according to the CES[34] database.

three different regimes. The original form of the deformation map displayed in **Figure 1** was derived by Spaepen in 1977 on the basis of the free-volume theory,[9] but has been modified and expanded numerous times. We will adapt a version similar to the one designed by Schuh and co-workers.[5] In direct comparison with a deformation map of crystalline metals that contains several dominating mechanisms at different stress, temperature and strain-rate conditions, it is worth to note that a single atomistic deformation mechanism is sufficient to describe the three different regimes in Figure 1. Depending on temperature (here normalized with the glass transition temperature T_g), shear stress τ (normalized with the shear modulus μ), and applied strain rate $\dot{\varepsilon}$, MGs deform elastically (region I), inhomogenously (region II), or homogenously (region III, containing both Newtonian and Non-Newtonian flow).

Figure 1 contains a wealth of interesting information, and the boundaries between the different regimes should be understood as variable upon various influencing parameters (plastic strain ε, $\dot{\varepsilon}$, T, applied pressure, ...). For example, the transition between elastic and homogenous flow as a function of temperature is strain-rate dependent—higher rates extend region I to higher normalized temperatures. A MG can similarly deform inhomogenously under high enough strain rates at $T/T_g > 1$[29] (not shown in Figure 1), and an external pressure shifts the transition between elastic and inhomogeneous flow to higher τ/μ.[31] Of highest relevance in this report is regime II that indicates the stress-temperature domain of shear-band mediated plastic flow of MGs. It has to be noted that τ should be understood as a global stress under ideal loading conditions, because shear bands are known to also form at stresses well below $\tau/\mu = 10^{-2}$,[32] due to stress concentrations in virtually any realistic experiment. Nevertheless, macroscopic plastic strain due to shear-banding in region II sets in at a well reproducible yield stress,[33] which is at odds with the typical semantics that MGs are brittle. In fact, malleable MGs in compression may have a Weibull modulus (≈70) comparable with that of strain-hardening ductile crystalline metals,[33] strongly indicating that yield is an intrinsic property. This reproducible yield stress at an elastic strain, ε_{el}, of ≈2% directly reflects the most striking advantage of MGs over conventional crystalline structural materials. The high elastic-strain limit, in combination with high yield stresses, places MGs as an exceptionally performing structural material in a strength-elasticity chart (**Figure 2**), and allows for stored elastic energies per unit volume, $U_{el,V}$, of the order of $U_{el,V} = 0.5 \times E\varepsilon_{el}^2 \approx 2 \times 10^7$ J m^{-3}, using an elastic modulus, E, of 100 GPa. This is at least a 4 times higher elastic energy density than a high-performing steel can store.

Figure 2 represents the practical limit at the macroscopic scale. At the microscopic level, the strength level is maintained, and strain levels of more than 3% can be reached.[35] However, this high capability of storing elastic energy is counteracted by a limited ductility and virtually no strain hardening—properties that are indispensible for most structural applications. In fact, when loading MGs with a testing system of typical laboratory compliance most MGs exhibit failure in tension upon the formation of the first shear band, whereas some MGs are malleable in compression or under mixed deformation modes.[5] There is thus a high interest in designing MGs that can deform plastically with some degree of stable flow stress, which motivates research on shear bands in general.

3. Selected Aspects Regarding Shear Bands in Metallic Glasses

Depending on the loading mode and nature of the evolving stress field during plastic deformation, MGs develop at least one, but more often a high number of shear bands, for which the most obvious evidence is a nm to μm large shear offset. **Figure 3** shows scanning electron microscopy (SEM) images of shear-band morphologies obtained from nominally uniaxial compression testing of a Zr-based ($Zr_{52.5}Ti_5Cu_{17.9}Ni_{14.6}Al_{10}$, Vit105) MG. The figure demonstrates in (a) the often found dense morphology with numerous shear bands nucleating at

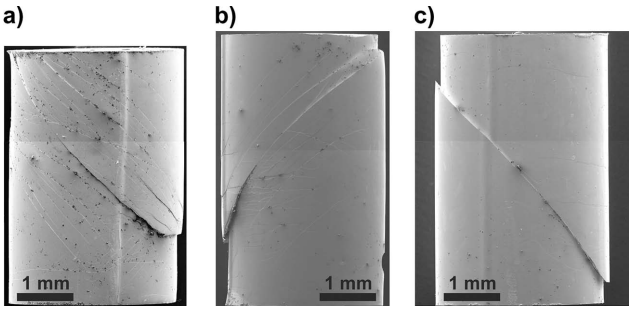

Figure 3. Possible shear-band morphologies after compression tests of MGs, imaged via SEM. a) A slightly misaligned compression sample yields a dense shear-band structure with shear bands nucleating predominantly at the anvil-sample interface. b,c) Examples of shear-band nucleation apart from the anvil-sample interface, allowing for unconstrained flow.

the sample-anvil interface, whereas in (c) all plastic strain was mediated by one shear band and (b) represents an intermediate case. These various shear-band evolutions can only be explained by differences in the degree of confinement.[33,36,37]

The density of the shear-band morphology scales well with the achievable plastic strain, because strain is distributed over a larger number of active shear planes, which is first indirect evidence for structural changes during flow of a shear band. Flow localization as a consequence of structural softening is believed to be either due to shear-band heating or a shear-induced dilatational mechanism. Shear-band heating was suggested to occur as an adiabatic process.[38] Crucial for a correct determination of the heat development is the time of the shear-banding process, which was assumed to range between ns and μs and therefore a temperature rise of up to several 1000 K was suggested.[39] A first sufficiently well time-resolved experiment by Wright and co-workers yielded time scales of a few ms for shear-band operations in $Pd_{40}Ni_{40}P_{20}$.[40] Based on this, a temperature rise of only a few degrees K can be estimated. We note that the often displayed vein patterns on the fracture surface of a MG are not due to a shear-banding mechanism, but arise during failure upon which all elastically stored energy is released at once.[41] It is thus clear that shear-band heating cannot be the cause for structural softening and a subsequent near-autocatalytic failure mechanism. Instead, its origin has to be found in a stress-induced structural change. Numerous techniques have been used to probe the structural difference between undeformed MGs and MGs containing shear bands. The most consistent observation is an increased degree of disordering and an increase in free volume (lower atomic or electron density), which was derived from X-ray techniques,[42] positron annihilation,[43] or neutron diffraction.[44] Transmission electron microscopy (TEM) even allows to directly probe the scale of shear-band thickness,[45] which is typically assigned to be ≈20 nm,[46] even though direct evidence is rare and controversial. Some authors report free-volume coalescence into nm voids[47] and subsequent nano-crack formation[48] upon shear banding, whereas other studies cannot support void formation using phase-contrast TEM.[49] Using in situ TEM experiments, Wilde and Rösner were able to observe structural changes in a $Al_{88}Y_7Fe_5$-glass after straining.[50] At ambient conditions, high-resolution TEM revealed distinguishable bright-field contrasts between the matrix and the shear-band region, but more interestingly, preferential nano-crystallization occurred within the shear-band region upon mild heating with the electron beam. This result indicates an increase in atomic mobility upon thermal activation in the shear-band region, and supports the view of abundance of excess free volume in the shear band. Tracer-diffusion measurements in shear bands of a $Pd_{40}Ni_{40}P_{20}$ glass by the same group provided evidence for an increased diffusion coefficient from 10^{-25} m^2 s^{-1} in the undeformed matrix to 10^{-17} m^2 s^{-1} in the shear band.[51] Again, the large difference in diffusion coefficients between the matrix and the shear-band material clearly indicates a significantly altered atomic structure inside the shear band even long after the actual deformation experiment. Direct nano-mechanical probing of shear bands by Pan et al. supports this structural change via a significant reduction (≈36%) in hardness and a derived volume dilatation of about 1.14%.[52] The most intriguing result of the study by Pan et al.[52] is the finding of a micrometer-wide affected zone, confuting the traditional view of a shear band being confined to some tens of nm in width.[46] Further evidence for a micro-scale signature of a single shear band was found in Maass et at.,[53] where the origin is discussed in terms of internally developing stress fields along the shear-band line. Independent of the shear-band width, one must thus conclude that during plastic flow there is an ample softening of the shear-band material, which leaves a signature of increased disordering, higher atomic mobility, internal stresses, and mechanical softening for a shear band after activation. Simulations indicate a similar picture, where recent explorations of the potential energy landscape of the glassy structure reveal a shift of the transition energy distribution to lower values after simulated deformation.[26] In fact, modifications of the potential energy landscape due to an applied stress argue that the material inside the shear band is undergoing a stress-induced glass transition,[54] which is supported by many more modeling efforts all exhaustively outlined in a recent review on shear bands in MGs.[55] While the above-outlined selected studies provide strong evidence for a structural change of the shear band relative to the matrix, the actual nature of shear-banding will continue to be a topic of intense research and needs to be assessed when the shear band is active, that is, in its dynamic state.

4. Shear-Band Dynamics in Metallic Glasses

During plastic straining of a MG, may it be a macroscopic or a micrometer-sized sample, the dynamics of shear-band operations can qualitatively be divided into two types, both linked to their corresponding apparent stress-strain behavior in the inhomogeneous deformation regime. Depending on the applied strain rate or testing temperature, MGs exhibit intermittent activation of shear bands, which yields either a jerky stress-strain curve, or apparent smooth flow. **Figure 4**a displays these two flow behaviors, which are termed serrated (25 °C, $\dot{\varepsilon} = 10^{-3}$ s^{-1}) or non-serrated flow (–100 °C, $\dot{\varepsilon} = 10^{-3}$ s^{-1}). Both curves are obtained during displacement-controlled straining, which results in fast stress drops during serrated flow as indicated in the left inset. At room temperature, a stress drop occurs within ≈1 ms, and

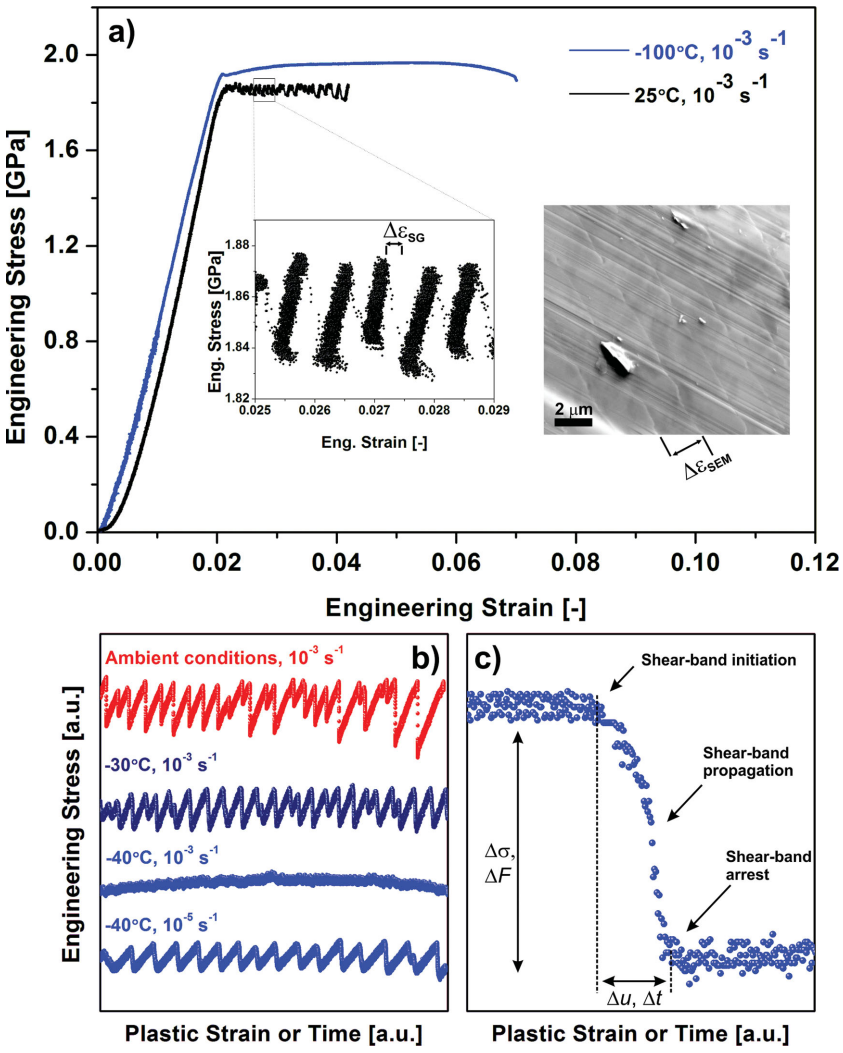

Figure 4. a) A serrated (25 °C, $\dot{\varepsilon} = 10^{-3}$ s^{-1}) and non-serrated (–100 °C, $\dot{\varepsilon} = 10^{-3}$ s^{-1}) stress-strain curve of Vit105. The left inset shows a zoom-in of the serrated flow curve with the strain increment $\Delta\varepsilon_{SG}$ per serration. The right inset displays shear striations imaged by SEM with a step size $\Delta\varepsilon_{SEM}$ on the shear-surface originating from serrated flow. b) Extracts from flow curves of Vit105, illustrating the effect of strain rate and temperature on the flow behavior. c) One stress drop as a function of time with indications of the different shear-banding stages and the corresponding quantities $\Delta\sigma$ (or ΔF) and Δu (or Δt).

can therefore only be resolved properly with an adequate time resolution and hence data acquisition rate (DAR).[56] During each stress drop, a strain increment of $\Delta\varepsilon_{SG}$ is seen, where the subscript SG refers to the used strain gauge. This is the strain jump magnitude as caused by the elastic relaxation of the machine, whereas the total amount of strain for one serration also includes the conversion of elastic strain of the sample into plastic strain. This issue will be discussed in detail in Section 4.2. The consequence of both contributions is that the measured strain increment, $\Delta\varepsilon_{SEM}$ (right inset in Figure 4a), on the shear surface of the MG is larger than $\Delta\varepsilon_{SG}$. Finally we note that from an inspection of the shear-band morphology alone (see Figure 3), one could not decide whether one or the other inhomogeneous deformation mode of Figure 4a (i.e., serrated vs non-serrated flow) occurred.

Given the two stress-strain curves in Figure 4a, one may ask for the reason of this change in deformation mode. The transition between serrated and non-serrated flow is not new, and first pioneering work by Kimura et al. in the early 1980s[57] investigated the transition as a function of applied rate and temperature by qualitatively determining the moment upon which the stress drop magnitude, $\Delta\sigma$, becomes zero. As shown in Figure 4b, on average $\Delta\sigma$ decreases and eventually vanishes with decreasing temperature at a given applied rate ($\dot{\varepsilon} = 10^{-3}$s^{-1}; ambient conditions, $T = -30$ °C, and $T = -40$ °C). On the basis of this, Kimura and co-workers[57–59] demonstrated that the transition between serrated and non-serrated flow for MGs follows an Arrhenius-type equation, where the activation energies vary among different MGs ($E_A^{Pd} = 0.35$ eV, $E_A^{Ni} = 0.46$ eV, $E_A^{Co} = 0.48$ eV, metal-basis given in superscript). With this it was shown that the cross-over between the two inhomogeneous flow modes is linked to a structural mechanism that is thermally activated and therefore rate-sensitive.

Instead of only focusing on the qualitative appearance of the stress-strain response, a close inspection of a single elastic loading and subsequent stress-drop cycle (Figure 4c) suggests that there are several stages: a shear-band initiation at the peak stress, a shear-propagation phase during which $\Delta\varepsilon$ is generated, and an end-stress where shear-banding stops and after which elastic loading sets in again. The SEM image in the inset of Figure 4a supports the repeated activation of the shear band, where each cycle leaves faint lines on the shear-surface that should not be confused with the facture surface. Thus, the quantities of interest are a stress or force drop magnitude, $\Delta\sigma$ or ΔF, a displacement magnitude Δu, and the time Δt during which the process takes place. These properties shall be subject of the following sections in order to characterize the dynamic stages of shear-banding: initiation (Section 4.1) – propagation (Section 4.2) – arrest (Section 4.3).

Before addressing details related to these shear-banding stages, some insightful comparisons between the rate- and temperature-dependent stress-drop amplitude (Figure 4b) and other materials systems can be made. Serrated flow of MGs resembles a stick-slip behavior known for many types of materials and processes across multiple length scales.[60] Those span from nm in macromolecular fluids to cm in plate tectonics, most commonly visualized with a block-slider setup and a drive system attached with a spring.[61] While the underlying physical mechanisms of the repeated stick-slip movements of the two interfaces are specific for each system, they all have in common that some elastic energy from the sample-spring assembly is released during sliding.

Stick-slip motion and thus serrated flow are therefore absent in an infinitely stiff mechanical system, which is impossible to achieve in MG testing due to the finite compliance of the sample. In addition, the force-drop amplitude in stick-slip systems is known to decrease with increasing applied drive-velocity, where the base stress remains the same but the peak stress depends on the applied drive-velocity. This dynamic weakening effect is also seen in MGs, as evidenced in Figure 4b ($T = -40$ °C; $\dot{\varepsilon} = 10^{-5}$ s^{-1} and $\dot{\varepsilon} = 10^{-3}$ s^{-1}). Earlier studies interpreted this effect as a basis for a negative strain-rate sensitivity.[62,63] In this article this will be related to the time scales of competing processes within the shear band, which upon increasing the applied drive will have less time to strengthen statically. This will decrease the peak stress (force) prior to reentering the slip state. It is hence the stick state that accounts for static strengthening and therefore the stress (force) drop magnitude. This will be further discussed in Section 4.3 (Shear-Band Creep, Arrest and Aging). When the drive velocity is increased such that the stick-slip regime is left, dynamic strengthening can be observed in a block-slider system. Now sliding proceeds at a velocity-dependent force (also interpreted as a positive strain-rate sensitivity), which qualitatively is inferred from high strain-rate or low-temperature testing of MGs.[63]

With the rich body of analogies between stick-slip phenomena of, in particular, granular disordered systems and MGs, many experiments can be motivated to gain direct insight into the dynamic properties of shear-banding and to shed light onto atomistic processes that govern the relationship between serrated and non-serrated flow. Being far from the first attempt to characterize the dynamics and confinement of flow in MGs, the following body of summarized experiments relies on high data-sampling rates during all stages of shear-banding. This in situ insight of the dynamics greatly enhances our understanding of inhomogeneous flow in MGs.

4.1. Shear-Band Initiation

The initiation phase of a shear band in MGs is hidden in the peak-stress regime in Figure 4c. From this it can be deduced that the time scale of shear-band initiation should be in the far sub-ms range, under the assumption that initiation is a process that precedes propagation. Furthermore, the stress and strain signal does not resolve any specific feature at the onset of propagation (stress drop) that foreshadows shear-band initiation. The questions that naturally emerge are: i) What could be the physical process of shear-band initiation?, and ii) what is the experimental method that is sensitive enough to capture initiation? In soil mechanics it is a long-known fact that the application of shear induces a volume expansion in the region of strain localization. In fact, time-resolved stick-slip friction experiments of shearing granular materials provide direct evidence of a volume dilation prior to slip. **Figure 5** reproduces experimental data of Nasuno and co-workers,[64] who apart from the horizontal velocity of the slider-setup also recorded the vertical displacement of the horizontally shearing interface. Strikingly, Figure 5 demonstrates that there is a maximum in vertical displacement prior to the peak velocity of the horizontal slip movement, and that the maximum horizontal acceleration correlates well with the maximum vertical displacement. In addition, Nasuno et al.[64] found that the maximum vertical displacement, and thus dilation of the shearing material, is about 10% of the mean particle diameter.

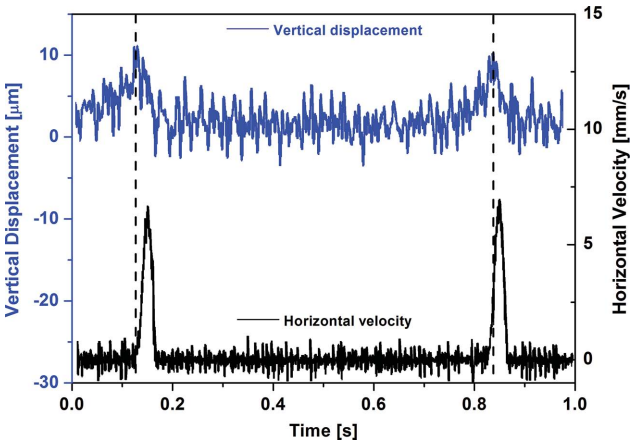

Figure 5. Vertical displacement (upper data) and horizontal velocity (lower data) of the top plate in a block-slider experiment of spherical glass particles as a function of time. Reprinted with permission.[64] Copyright 1998, American Physical Society.

Projecting these findings onto MGs, it becomes evident that it is unlikely to record a signature of vertical dilation with any available strain-gauging method, because ≈10% of the average Goldschmidt radius would be less than 1 Å. However, the application of an independent probe that can capture the signature of dilation with μs resolution identifies in situ acoustic emission (AE) as the method of choice for probing shear-band initiation of MGs. For details on the experimental set-up, we refer to the work of Klaumünzer et al.[65] Indeed, when recording the AE-signal during a compression experiment of a Zr-based MG ($Zr_{52.5}Ti_5Cu_{17.9}Ni_{14.6}Al_{10}$), distinct amplitude pulses can be observed concomitantly with load drops during serrated flow.[65,66] Paying carefully attention that the time synchronization between the AE-signal and the stress-strain data is precise, it becomes clear that the peak amplitude of the AE-pulse is attained before the stress has dropped and the displacement has increased noticeably. **Figure 6** displays a selected stress drop and the corresponding AE data-stream recorded at a DAR of 2 MHz.

Adding the time line of the axial strain evidences a comparable picture to what is seen for granular media in Figure 5, with the difference that there is virtually no detectable change in axial strain (and thus displacement velocity) at the moment the AE-pulse is recorded (Figure 6). In the related analysis, only the AE-pulse rise time is considered because the decaying signal after the peak amplitude is attributed to vibrations and reflections within the sensor. Analyzing the mean rise-time of the AE-pulse at room temperature is indicative of an initiation process with a duration of around 25 μs, which represents the mean of all investigated pulses at the onset of the stress drops within one stress-strain curve. Not having addressed the possible underlying source mechanism to the rising part of the AE-pulse, we note that theoretical analysis suggests that the shear-band propagation speed is too low to be captured by AE.[67] Furthermore, when considering shear-softening and a related decrease in viscosity, AE-studies as a function of temperature covering the transition between inhomogeneous and

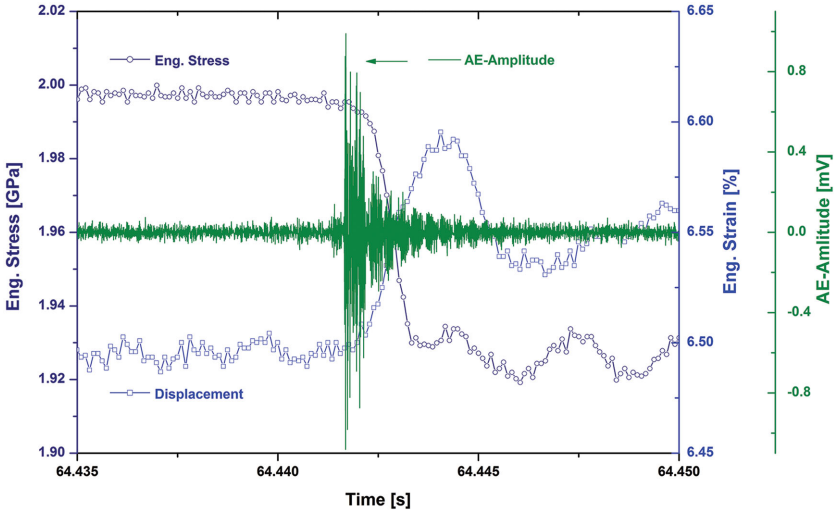

Figure 6. Stress drop and acoustic emission amplitude as a function of time for a Vit105 metallic glass tested at –10 °C at a strain rate of $\dot{\varepsilon} = 10^{-3}$ s^{-1} (serrated flow regime). The emitted pulse appears at the onset of the stress drop. The corresponding jump in strain is also shown.

homogeneous flow reveal a disappearance of AE-pulses when the homogeneous regime is reached.[68] That means, AE-sources are absent when viscous shear sets in, which is another reason why at this stage the decay signal is not interpreted in terms of a physical shear-banding mechanism.

Relating the occurrence of the AE-pulse to an underlying physical mechanism is not trivial. Nevertheless, the good agreement of the results between granular materials and the studied MGs strengthens the presupposition that dilation occurs initially. A volume expansion is therefore seen as a precursor event to shear-band propagation, while this does not imply that dilatation is required to be present throughout the entire subsequent propagation stage. With the motivated working hypothesis of a structural dilatation upon shear-band initiation, a dilatational AE-source model can be used to quantitatively analyze the response seen in Figure 6. The model was proposed by Scruby et al.,[69] and includes a point source in an infinite elastic medium. In doing so, an expression can be derived for the surface displacement due to an elastic wave emitted from the point source. Adapting this formalism to the experimental setup and material used, the volume expansion δV is found to be proportional to the rise time t_r of the AE-pulse and its amplitude U_p: $\delta V = \frac{1}{C}\int_{t'}^{t'+t_r} u(t)\,\mathrm{d}t \approx \frac{1}{2C} t_r U_p k_f$, with C being a constant and k_f a sensor calibration factor. Via an additional set of materials and geometrical factors, all outlined by Klaumünzer et al.,[65] the change in volume related to shear-band initiation can be derived. For a number of AE-pulses (≈80 pulses), and hence shear-band initiation processes, the obtained volume change $\delta V/V_{SB}$ is calculated using a shear-band thickness of 15 nm. The distribution of $\delta V/V_{SB}$ obtained from the various AE-pulses is summarized in **Figure 7**.

The most striking feature of Figure 7 are the very low values of $\delta V/V_{SB}$, not exceeding 8.5% and having a median of around 2%. These values are noticeably lower than typically reported estimates also indicated in Figure 7. For example, Donovan and Stobbs derived about 10% atomic volume dilation,[45] and Argon et al. deduced an average value of up to 50%.[70,71] This raises the question of how these differences can be explained. The most straightforward answer is that all of the other studies are conducted ex situ long after the active shear-banding process, a fact that Donovan and Stobbs themselves discuss in the context of the sensitivity of their TEM technique. Argon and co-workers argue that the high value of more than 50% can only be explained by larger than atomic-size void formation, an argument that finds support by the earlier work of Pampillo et al.[73] While the details of the various experimental techniques offer a multitude of reasons to explain the discrepancies to our measured values in Klaumünzer et al.,[65] we emphasize that Figure 7 constitutes so far the first in situ measurement of the dilation process that accompanies shear-band initiation. We also reemphasize that the dilation derived on the basis of the AE-experiments is only attributed to the initiation stage. This on the other hand means that the dilatation reported by the authors cited in Figure 7 may result from the flow process rather than shear-band initiation.

As a further step of analysis and interpretation of the values in Figure 7, it is possible to link the volume expansion $\delta V/V_{SB}$ to the free volume within a shear band. According to Cohen and Turnbull,[74] the free volume content, $V_f(T)$ for $T > T_g$, of a MG is described by the form $V_f(T) = V_0 + V_m(\alpha_l - \alpha_g)(T - T_g)$, where V_0 is the free volume at or below T_g, V_m is the molar volume, and α is the thermal volume expansion coefficient

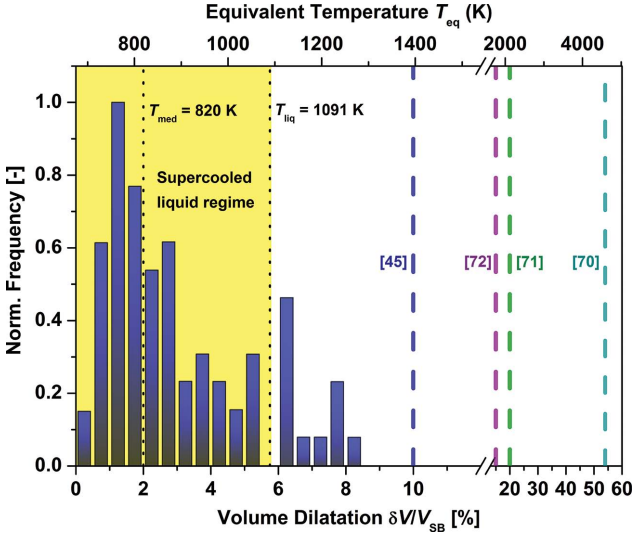

Figure 7. Histogram of volume dilatations $\delta V / V_{SB}$ obtained from AE-pulses within the serrated flow regime for Vit105.[65] The majority of the $\delta V / V_{SB}$ values falls within the domain of the equivalent supercooled liquid regime. All vertical dashed lines indicate values from previous ex situ works,[45,70–72] and the vertical dotted lines (T_{med} = 820 K and T_{liq} = 1091 K) show the equivalent temperature for the median volume dilatation and the equivalent liquidus temperature.

of the liquid (l) and glass (g), respectively. It is noted that the unrestricted use of $V_f(T)$ above T_g is approximative, as the original description was developed for a temperature near the glass transition. With this approach one can ask what the corresponding equivalent temperature T_{eq} above T_g would be to generate the required amount of free volume $\Delta V_f = V_f\left(T_{eq}\right) - V_0$ equivalent to the amount of $\delta V/V_{SB}$ as derived from the AE-measurements. For this, δV obtained with AE is normalized to the number of atoms in the shear band V_{SB}/V_m. It is now possible to derive that $T_{eq} - T_g = \left(\delta V / V_{SB}\right)\left(1/(\alpha_l - \alpha_g)\right)$,[65] of which T_{eq} is added as an upper x-axis in Figure 7. With $T_{eq} > T_g$ (T_g = 675 K in the case of Vit105) and the liquidus temperature T_{liq} = 1091 K, the majority of the data in Figure 7 falls within the first 200 K above T_g, i.e., within the supercooled liquid regime. From this one can conclude that the structural dilatation during shear-band formation is equivalent to a state in the supercooled liquid regime—a result that finds strong support by theoretical work showing that shear-band formation can be understood as a stress-induced glass transition.[54] It is further of interest to compare the range and thus scatter covered by the $\delta V/V_{SB}$-values in Figure 7 to recent findings using high-angle annular dark field TEM.[75] In this work, the authors find variations of both positive and negative density changes between ca. +6 and –10%. The data in Figure 7 can only represent the dilatational part of the findings by Rösner et al,[75] but is of very good agreement in both range and absolute magnitude.

The experimental data contained in Figures 6 and 7 are obtained from the overall shear-band initiation process, without allowing to further extract a model for how the dilation proceeds within the material. Two scenarios are possible, of which the first is the emergence of an increased activity of local structural transitions on the plane with the highest resolved shear-stress leading to a percolative formation of the softened shear-plane. The second model picture involves a rejuvenating front that nucleates from a particular site on the later formed planar defect. Both of these models are reminiscent of homogenous[76] and heterogeneous shear-band nucleation,[77] respectively, and are observed in computer simulations, with the important difference that in homogeneous shear-band nucleation no resolvable strain is mediated by the nucleation process, as clearly supported by the experimental results. In more detail, mesoscale STZ-simulations performed by Homer[78] describe shear-band initiation stages, where an STZ-cluster develops into a nascent shear-band, with a propagation front that reaches its maximum length at the very early portion of the stress drop, compatible with Figure 6, and subsequently thickens. Assuming that the rejuvenation front propagates with ≈10% of the transverse sound velocity of ~10^2 m s^{-1},[79] and knowing the maximum shear-plane diameter (≈4.5 mm), indeed yields a formation time of some tens of µs, consistent with the AE-experiments. Nevertheless, an experimental distinction between the two shear-band nucleation models cannot be made. The now formed shear band will propagate and form a shear offset, as will be discussed in the following section.

4.2. Shear-Band Propagation

Before highlighting the details of shear-band propagation, some critical questions have to be asked. Firstly, is it reasonable to assume that one serration (stress drop and displacement jump) corresponds to the operation of one shear-band? Secondly, does shear-band propagation occur via a moving front or the sliding of two parallel surfaces? Verifying that one serration is linked to the operation of one shear band can be done by polishing a rectangular prism compression specimen that is subsequently deformed to a strain of one single stress drop. Afterwards all four sample surfaces are imaged by SEM to document the shear-band morphology, the shear surface and the shear offset. Reactivation of the same shear band and the generation of an additional single stress drop indeed reveals that a single serration can exclusively be linked to the activation of one shear band. This iterative procedure was followed by Maass et al.[80] The second question has been answered via high-speed imaging experiments using the knowledge that the typical time scale for shear propagation at room temperature is in the ms range. Both Song et al.[81] and Wright et al.[82] have convincingly shown that localized shear occurs in a simultaneous fashion across the entire plane, and not in a progressive manner. Wright and co-workers also found that shear sliding is coincident with the load drop of a serration, supporting the iterative SEM-based procedure used to answer question 1.

With this knowledge and an experimental set-up that is characterized by acquiring data at timescales shorter than the shear-band dynamics, the spatio-temporal properties can be readily assessed. Details on the used set-up can be found in the literature.[66,80,83] Using displacement data, such as those shown in Figure 4c, converting them to shear displacement and differentiating them with respect to time yields a velocity profile as a function of time for the propagation event (**Figure 8**a).

This velocity profile has a distinct characteristic of an acceleration and deceleration phase, but steady-state sliding does not exist. Both propagation phases span approximately the same amount of time and displacement, as can be deduced from the symmetry of the profile. The data in Figure 8a show that shear-band propagation at –30 °C proceeds with peak velocities of several tens of µm s^{-1}. It is instructive to plot the corresponding stress-drop profile (Figure 8b), which evidences that the peak velocity is consistently reached at half the stress drop, irrespective of the stress-drop magnitude. Thus, larger stress drops or displacement jumps are propagating faster, which holds true during all serrated flow conditions (across both $\dot{\varepsilon}$ and T). Additionally, there is a correlation between $\mathrm{d}\sigma/dt$ or $\mathrm{d}u/dt$ and the flow stress or the total plastic strain at which a serration occurs (not shown here). In particular, the strain dependence is a direct signature of structural changes within one shear band; a fact that so far is largely unexplored.

Whereas both the influence of plastic strain and flow stress complicate the analysis of shear-band dynamics, the temperature-dependent trends that will be discussed in the following are remarkably robust. In fact, careful analysis of shear-band velocities from samples deforming strongly constrained with a dense shear-band morphology (Figure 3a) and those shearing on a single unconstrained shear-plane (Figure 3c) evidence the same temperature-dependent shear-band dynamics.[80,84] This means that the derived shear-band velocities may scatter more for a sample deforming under constrained conditions, because of the larger spread in stress-drop magnitudes, but the temperature-dependent shear-dynamics is on average unaffected.

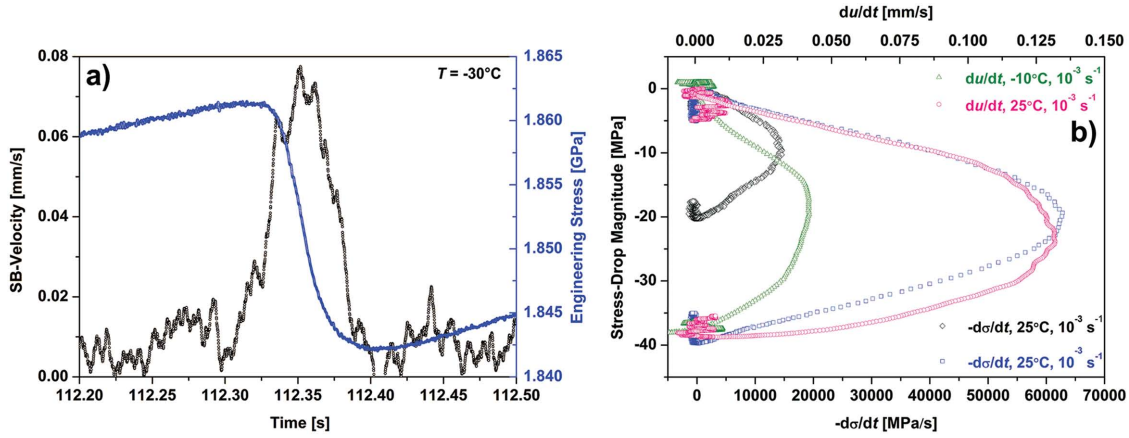

Figure 8. a) Shear-band propagation velocity and corresponding stress drop as a function of time (–30°C, $\dot{\varepsilon} = 10^{-3}$ s^{-1}). The peak velocity is attained at ca. half the stress-drop magnitude. This is clearer seen in (b), where the stress-drop magnitude $\Delta\sigma$ as a function of axial velocity du/dt is shown (T = 25 °C and –10 °C, $\dot{\varepsilon} = 10^{-3}$ s^{-1}). The panel (b) also displays $\Delta\sigma$ as a function of the stress-relaxation rate $-d\sigma/dt$ for two stress drops. Smaller stress drops attain lower maximum axial velocities and lower stress-relaxation rates at constant temperature.

Before investigating the shear-band dynamics in more detail, we recall that high-speed imaging of the shear-dynamics at room temperature evidenced a continuous sliding mechanism[81,82] with two sample parts translating relative to each other separated by the shear-band layer—a low-viscous layer (~10^5 Pa s at RT, using $\eta = \tau w / v_{SB}$, with τ the shear-stress, w the shear-band thickness (≈20 nm), and v_{SB} the shear-band velocity), which is presumably in a similar state as would be the bulk material in the supercooled liquid regime.[66,85] The latter is also supported by the in situ AE-measurements (Figure 7) and compatible with theoretical studies.[54]

The average shear-band velocity for each individual serration, v_{SB}, can now be expressed by $v_{SB} = \sqrt{2} \times (\Delta u_0 + \Delta F C_S)/\Delta t$, where $\sqrt{2}$ is a geometrical factor taking into account the angle between shear-plane and loading axis, Δu_0 is the measured displacement jump, ΔF is the force drop magnitude, C_S is the sample compliance, and Δt is the elapsed time of the instability. It is important to understand that v_{SB} is a function of both the sample compliance and the machine compliance, which is contained in the measured value of $\Delta u_0 = \Delta F C_M$, with C_M being the machine compliance. Thus, the derived shear-displacement jump velocity, in the following termed shear-band velocity, is a property that will depend on the coupled mechanics of the sample and machine, where the compliances of both parts are determining v_{SB}.[79,80,86] At the limit of $C_{M,S} \rightarrow 0$, serrations would be absent—a scenario that is practically impossible, since finite sample and machine compliances always remain. This consideration holds true to any mechanically coupled system that exhibits instabilities, leading to the conclusion that the numerical value of the derived shear-band velocity is not intrinsic to the material. Nevertheless, and as will be shown in the following, trends as a function of other external parameters or structural variations will allow great insights into the underlying dynamics and physics of intermittent shear-band plasticity.

As evident from Figure 8b, there is a significant effect of temperature on the stress-velocity profiles. That is, the shear process slows down considerably upon decreasing the temperature. As such this is not surprising, because i) it is an established fact that plasticity of metallic glasses is thermally activated, also being the essence of Figure 1, and ii) the underlying lower viscous state within the shear band is expected to obey some exponential viscosity law. The in-depth analysis of this temperature dependence allowed us for the first time to directly assess shear-band plasticity in real time,[37,65,66,80,83,87] avoiding post-mortem investigations that may be obscured by structural relaxation processes taking place after the actual process of interest. **Figure 9** summarizes the shear-band velocity as a function of inverse temperature for two different alloy systems, namely $Zr_{52.5}Ti_5Cu_{17.9}Ni_{14.6}Al_{10}$ (Vit105)[80] and $Zr_{55}Cu_{35}Al_{10}$.[84] In both cases, v_{SB}, as obtained from the serrated flow regime, exhibits a linearly decreasing trend in the Arrhenius representation, which is indicative of a thermally activated shear-propagation process. The corresponding apparent activation energies for shear propagation, Q_{prop}, are 0.32 ± 0.01 eV and 0.35 ± 0.04 eV, respectively, for the two alloy systems.

The linear trends seen in Figure 9 can be observed irrespective of the type of MG alloy as long as a sufficient number of serrations can be obtained during plastic flow. Furthermore, Q_{prop} has been shown to be sensitive to chemical alloy composition and increases with increasing Zr-content in the $Zr_{55}Cu_{35}Al_{10}$ system.[84] The question that now arises is what these activation energies represent. It is clear that Q_{prop} indicates the resistance to shear-propagation, as can be deduced when comparing shear velocities at a given temperature across compositional variations within one alloy system: the lower Q_{prop} is the faster is the shear-band velocity at a given temperature. This is very much in agreement with the general atomistic picture of the characteristic (inelastic) shear rate for a collective local plastic transition (STZ), which typically is assumed to have any form of type $\dot{\gamma} = \dot{\gamma}_0 \times \exp\left[-Q / k_B T\right] \propto v_{SB}$, where $\dot{\gamma}_0$ is an average attempt frequency and the barrier energy Q is a function of parameters, normally including an intrinsic barrier height, a local shear stress biasing the intrinsic barrier, an average STZ activation volume, and/or other constants. We note that the barrier energy of some tenths of an eV is much lower than the typically assumed values for STZs (≈1–4 eV),[89] which can be understood when considering that Q_{prop} is a value of significance for the entire term in

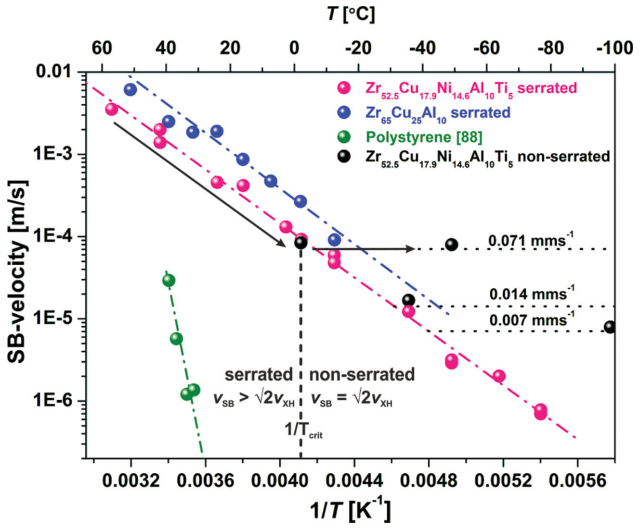

Figure 9. Shear-band velocity as a function of inverse testing temperature for two different Zr-based alloy systems[80,84] and for polystyrene taken from the literature.[88] The dot-dashed lines are fits to the data, the horizontal dotted lines indicate the resolved applied anvil velocity, v_{XH}, of the testing machine, and the vertical dashed line represents the boundary between serrated and non-serrated flow at a critical temperature T_{crit} and an applied anvil speed of 0.071 mm s^{-1}. At T_{crit} the anvil and the shear band move at the same speed, and below T_{crit} the shear band is driven at the speed of the machine giving rise to non-serrated flow. Lowering the machine velocity yields again non-serrated flow up to the temperature where the horizontal machine velocity line intersects the Arrhenius trend of the data.

the numerator of the exponential including the reduction due to stress biasing. Furthermore, Q_{prop} should be regarded as a mean barrier energy in a highly non-equilibrium state, and recent computer simulations and theories have suggested that the excitation energy for a local plastic transition, as well as the frequency prefactor, $\dot{\gamma}_0$, have broad distributions[90]—a result that is expected in the view of an extensive number of possible transition pathways for local structural excitations. A direct outcome of the continuation of our work in Thurnheer et al.[84] is the recent finding that Q_{prop} can be linked to the bonding strength of the fastest diffusor (in that case, Cu) with its surrounding atoms. This will be part of a forthcoming study.[91]

Upon closer inspection of Figure 9, it is recognized that the temperature-dependent nature of shear-band propagation has the same basis as earlier reports which show that the transition between serrated and non-serrated flow is thermally activated.[57–59,62,63,92] These earlier works discussed the transition from serrated to non-serrated flow in the context of the rate of diffusive short-range rearrangements,[57] cooperative shearing of STZs,[62,63] and limitations in shear-band nucleation kinetics.[92] By directly assessing the shear-band propagation velocity, the transition between inhomogeneous serrated and inhomogenous non-serrated plastic flow is easily understood: as indicated in Figure 9, serrated flow occurs at a fixed applied and resolved forward machine velocity, $v_{XH,1}$, as long as one follows the Arrhenius trend line at temperatures above the intersection point with $v_{XH,1}$ = 0.071 mms^{-1}. Passing this point ($v_{XH,1}$; $T_{crit,1}$ = 0 °C) towards lower testing temperatures yields a constant v_{SB}, which equals $v_{XH,1}$ at all temperatures below $T_{crit,1}$, so that non-serrated flow occurs. Serrated flow can, however, be recovered by lowering the machine velocity to, for example, $v_{XH,2}$ = 0.007 mm s^{-1} (see Figure 9). This means that the transition between the two flow modes can be entirely described by the competition between the applied deformation velocity and the shear-band propagation velocity. The occurrence of one or the other at a fixed deformation velocity is governed by the critical temperature, T_{crit}, where both speeds are equal.[80] It is therefore understandable that earlier work investigating the transition from serrated to non-serrated flow on the basis of the appearance of the stress-strain curve yields similar activation energies.[58,59,62] Determining the critical temperature where both speeds are equal is thus a way of identifying a time scale of a structural relaxation mechanism that leads to structural freezing. This will be addressed later on in this article.

Finding that characteristic time scales are responsible for the transition in flow mode sheds further light on another strongly investigated aspect of MG plasticity. Based on treating shear-band nucleation as the rate-limiting process with respect to strain impartation, numerous studies concluded that non-serrated flow arises due to an increasing shear-band nucleation rate with decreasing temperature, leading to a higher shear-band density and thus larger plastic strain at failure.[93,94] However, investigations of shear-band propagation dynamics down to 77 K have shown that all plastic strain can be accommodated by one single shear-band sliding at an imposed rate during non-serrated flow.[37] Reasons for the increased shear-band density in earlier studies must thus be found elsewhere than in shear-band nucleation kinetics. Furthermore, the strength increase with decreasing temperature below T_{crit} follows the commonly reported universal trend, also in the case of one single active shear-band.[37] This means that the further the testing temperature decreases below T_{crit}, the higher is the effective shear resistance of the shear band. As a consequence, the strength increase with decreasing temperature below T_{crit} can be understood with a rate effect of a non-Newtonian media, as we indeed could model with a simple viscosity law.[37]

Knowing that shear-band initiation proceeds within µs and that propagation at room temperature has durations of ms, possible temperature rises in shear bands can be readily assessed. The main question is if an instantaneous heat development can lead to thermal softening of the shear-band material, or if mechanical work (shear) itself is sufficient to cause structural softening and subsequent runaway failure. Selected experimental thermal imaging studies have directly shown that temperature rises during plastic deformation are only of the order of a few degrees Kelvin.[95] This is in good agreement with the long timescales for shear-band propagation, which challenge considerations of adiabatic heating during shear (stable serrated/non-serrated flow), because heat diffusion into the surrounding matrix is fast enough. In fact, earlier estimates of shear-band heating were predominantly based on shear velocities of the order of ≈100 m s^{-1}[96] that largely exceed those summarized in Figure 9. The measured Arrhenius behavior is in addition striking evidence for thermally equilibrated propagation conditions, which demonstrate the dominance of the externally applied temperature. Since direct thermographic observations are limited to the time resolution of thermal cameras and are at its best on the order of the time scale of shear-band

propagation, the conclusion that localized heating cannot be the primary cause of flow localization may still only be valid when one ignores the shear-band initiation process. Despite the fact that it is unclear if initiation occurs as a propagating front or via simultaneous (percolative) dilatation across the shear-plane (Section 4.1), the current models describe the heat, H, generated during shear-banding as $H \propto \delta_{SO}$, with δ_{SO} being the shear-band offset.[39] Since we have shown that δ_{SO} is negligible during initiation, we deduce that mechanical work is predominantly converted into structural modifications also during initiation, and that similar to shear-band propagation, heating during initiation cannot be the primary origin for structural softening.

Finally we note that thermally activated propagation of shear bands is not unique to MGs, but has also been observed in other amorphous materials. Exemplarily, Figure 9 displays selected data taken from Kramer,[88] who investigated the propagation of shear bands in glassy polystyrene (PS). He found an activation energy that is nine times higher (≈2.8 ± 0.3 eV, with data extending to 10^{-8} m s^{-1} in Figure 9), as can be inferred from the slope of the data. Being much slower and having a higher resistance, it is important to note that shear bands in PS evolve by a front propagation mechanism,[88] and not by continuous shear-displacement as identified for MGs.[82] Since the activation barrier is, in the case of MGs, intimately linked to the atomistic mobility within the softened lower-viscous shear-band material and, in the case of polymeric glasses, to structural transitions of long molecular chains (molecular weight $\approx 3 \times 10^3$),[88] such differences are expected.

Having described shear-band initiation via a shear-dilation process that transforms the material within the shear band into a state equivalent to that of the undercooled liquid regime, and having subsequently investigated shear-band propagation dynamics, the question of why shear bands arrest remains. The answer to this question is partly hidden in the symmetric velocity profiles seen in Figure 8, and will be the subject of the following section.

4.3. Shear-Band Creep, Arrest, and Aging

The results above clearly indicate that shear propagation during inhomogeneous flow occurs under thermally equilibrated conditions, indicating that heat generation during shear is not the origin for the substantial softening of the shear-band material. Heat may be generated during the initiation phase, but is expected to quickly dissipate into the matrix and will thus not dominate the shear-band propagation stage. It is now the question which mechanism allows sustained serrated compressive flow; or, in other words, which mechanism prevents catastrophic failure after only one serration, and why does the stabilizing process eventually ceases at failure? In what follows, it will be shown that structural re-strengthening, or aging, is one atomistic process that allows the shear band to repeatedly accommodate plastic strain. It will also be shown that static shear-band aging is proceeded by shear-band creep, and that aging can be thermally suppressed at low enough temperatures. Stop-and-go experiments in the non-serrated flow regime, as outlined below, allow us to assess aging time scales characteristic for the atomistic equilibration process during static re-strengthening.

Figure 8b clearly shows that deceleration sets in shortly before reaching the maximum shear-band velocity (where $d^2u/dt^2 = 0$). The deceleration is taken as evidence for a structural mechanism in the shear band that counteracts detrimental run-away propagation and leads to shear-band arrest. One way to characterize the deceleration in a controlled way is to drive the shear band during non-serrated flow, to subsequently stop the forward movement of the anvil, and to then probe the deceleration until no further changes in both, force or displacement, are resolved. This means, half of the velocity profile in Figure 8b can be investigated until the shear-band is arrested. Following arrest, after a certain waiting time Δt_w, the shear band can be again driven through the sample by a forward movement of the anvil. These so-called stop-and-go experiments generate iterations of dynamic and static states of the shear band. **Figure 10**a displays a typical stress-time curve together with a close-up view of a stop-and-go cycle. Several of such stop-and-go cycles were conducted during plastic flow of one sample, and different samples were tested as a function of temperature in the non-serrated regime. The inset in Figure 10a shows that subsequent to "stop" (while $\dot{\varepsilon}_{appl} = 0$) a stress relaxation $\Delta\sigma_r(\Delta t_w, T)$ is seen, and $\Delta\sigma(\Delta t_w, T)$ can be extracted following "start".

This behavior can be modeled quantitatively by effective temperature dynamics[20] based on STZ theory.[13,15] Introducing a

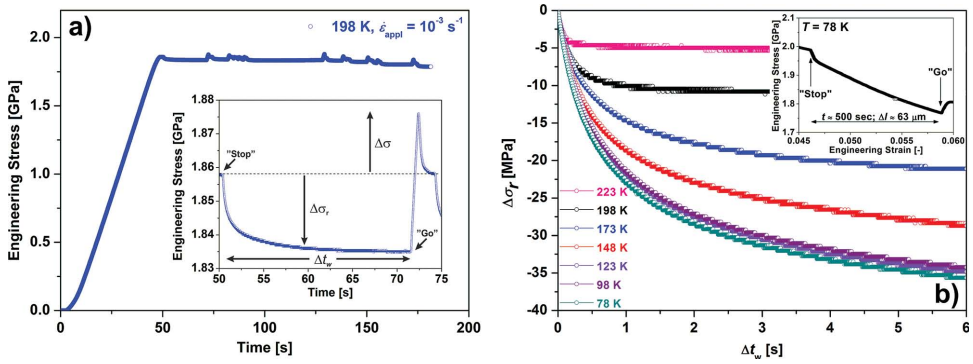

Figure 10. a) Stress-time curve of Vit105 (T = 198 K, 10^{-3} s^{-1}). The inset highlights the first stop-and-go cycle starting shortly after yield at 50 s and indicates the measureable quantities Δt_w, $\Delta\sigma_r$, and $\Delta\sigma$. b) Time-temperature dependence of the stress relaxation after stopping the experiment. The inset in b) evidences the absence of shear-band arrest upon stopping the movement of the anvil at 78 K.

thermally activated relaxation term, the effective temperature and stress decrease during each "stop" phase, during which also the number of available STZs decreases. Upon entering the "go" phase the stress needs to increase again to initiate plastic deformation, and the effective temperature correspondingly increases to its steady-state value.[20]

The time-temperature dependence of $\Delta\sigma_r$ is summarized in Figure 10b, evidencing that at high temperature, here 223 K, resolvable stress relaxation ceases after less than 1 s, whereas at 198 K stress relaxation is observed already for more than 2 s. Within the time span of Figure 10b there is no experimentally resolvable difference of $\Delta\sigma_r(\Delta t_w)$ for temperatures of 123 K and lower, suggesting that any temperature-assisted atomistic process that would facilitate structural freezing of the material within the shear band is thermally suppressed. This interpretation can be verified by recording plastic strain after stopping, of which a representative case for $T = 78$ K is displayed as an inset to Figure 10b. During the 500 s long stop segment, the strain increases continuously to in total 63 µm. This evidences a continued shear-propagation, which is entirely driven by the remaining static stress (while $\dot{\varepsilon}_{appl} = 0$), and supports the conclusion that within the experimentally accessible time scales of stop stages, shear-band arrest is suppressed at low temperatures (here $T < 123$ K). We note at this stage that these results indicate thermally activated mechanisms of the atomic dynamics in the shear band that allow for shear-band arrest, but that the latter should also depend on applied stress. As a consequence, $\Delta\sigma_r$ and $\Delta\sigma$ are at least functions of Δt_w, T, and the flow stress σ_f, of which the influence of σ_f is not assessed here.

Figure 11a now shows the stress overshoot magnitude $\Delta\sigma$ as a function of the waiting time for different temperatures between 148 K and 248 K. At all measured temperatures, $\Delta\sigma$ has a logarithmic waiting time dependence, which can be fitted (dashed lines) via $\Delta\sigma = A\ln(\Delta t_w/t_c)$, where A represents the logarithmic slope of the data in Figure 11a and t_c is the minimum waiting time to observe non-zero $\Delta\sigma$. It is seen that t_c shifts the data to longer waiting times with decreasing temperature. This means that at a given waiting time ($>t_c$) the overshoot magnitude, which represents an additional input of energy relative to the flow stress at "stop" to re-activate the shear band, strongly increases with increasing temperature. This directly indicates a static aging process of the material in the repeatedly re-activated shear-band, and is in good agreement with the interpretation on thermally suppressed shear-band arrest at very low temperatures (Figure 10b). It is expected that when $\Delta t_w \to \infty$, $\Delta\sigma$ approaches a constant value. Investigating this was, however, beyond the reach of the conducted experiments. We further note that for very small Δt_w, $\Delta\sigma$ is not expected to strictly converge to zero, as has been discussed for

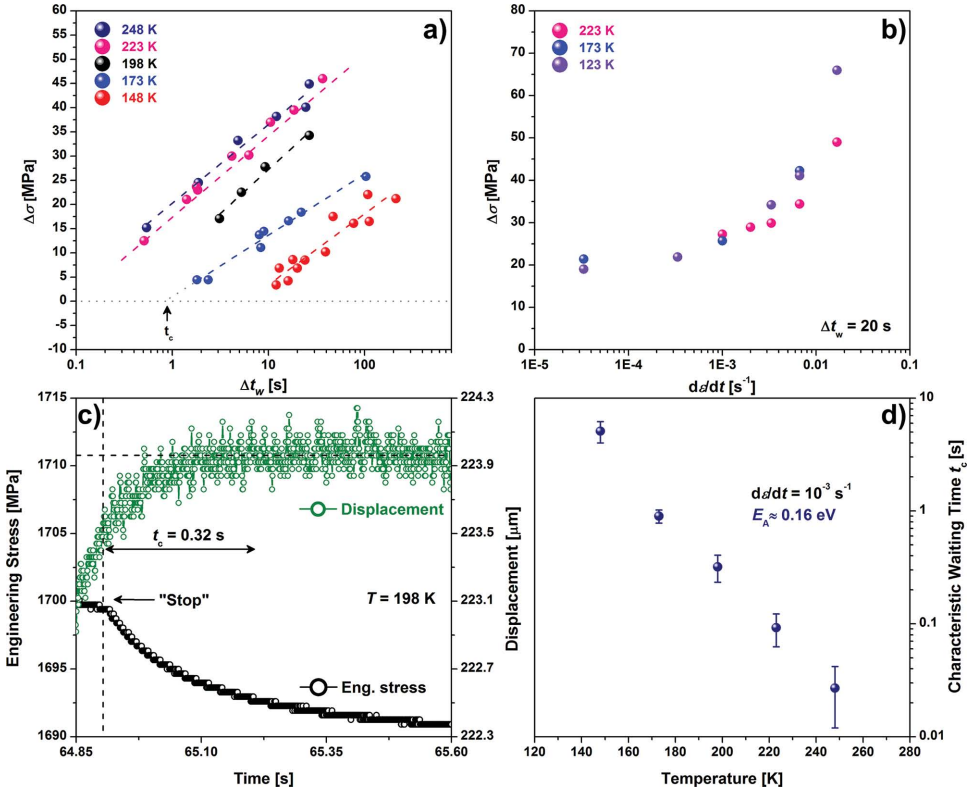

Figure 11. a) Stress-overshoot magnitude $\Delta\sigma$ as a function of waiting time and temperature. Linear fits to the data yield a characteristic time t_c where $\Delta\sigma$ tends towards 0. b) Stress-overshoot magnitude as a function of applied strain rate, performed at a constant waiting time of 20 s. c) Stress-time and displacement-time after "stop" measured at 198 K. The characteristic time $t_c = 0.32$ s, as derived from (a), is indicated and matches well with the time during which continued shear-band creep is observed. d) Characteristic waiting time t_c as a function of temperature. The data yield an activation energy for shear-band arrest, Q_{arr}, of about 0.16 eV.

other statically aging systems.[61,97] As shown in Figure 11b, $\Delta\sigma$ as a function of applied strain rate reveals no distinctly resolvable trend as a function of temperature: at a constant Δt_w (of 20 s), $\Delta\sigma$ increases with increasing applied strain rate more or less independent of temperature. Apparently, the faster the shear-band is driven prior to "stop", the stronger is the static aging of the material, overruling the temperature dependence of $\Delta\sigma$ revealed in Figure 11a.

With the above-presented empirical logarithmic aging law, t_c represents a characteristic waiting time required to structurally change the shear band from a liquid-like state to a solid-like state, which further ages when passing t_c. If this is truly the case, continued shear-band motion needs to be present during the time span between "stop" and t_c, which can be directly studied upon following the displacement signal (Figure 11c). It is indeed found that continued displacement can be resolved until a stable displacement level is reached at the characteristic time t_c. Therefore, Figure 11c appears to be a first direct measurement of shear-band creep in deforming amorphous alloys.

With the data of Section 4.2 demonstrating that shear-band propagation is a thermally activated process, and the fact that t_c is a measure of the continued shear-propagation prior to shear-band arrest, it can be assumed that the results in Figure 11a can be analyzed by setting $t_c(T) = B \times \exp\left(Q_{arr} / k_B T\right)$, where B is a prefactor and Q_{arr} is the apparent thermal activation barrier for shear-band arrest. Rewriting the logarithmic waiting time dependence of $\Delta\sigma$ yields $\Delta t_w(T, \Delta\sigma) = t_c(T) \times \exp\left(\Delta\sigma / A\right)$, which with inserting the assumed thermally activated characteristic time t_c gives $\Delta t_w(T, \Delta\sigma) = B \times \exp\left(Q_{arr} / k_B T\right) \times \exp\left(\Delta\sigma / A\right)$. A similar equation can be derived by studying effective temperature dynamics within STZ theory.[20] With $\Delta\sigma = 0$, $\Delta t_w \rightarrow t_c$, supporting the above assumption of an Arrhenius behavior of the characteristic waiting time t_c. A confirmation of this approach is shown in Figure 11d, which summarizes t_c as a function of testing temperature and allows for an estimate of the corresponding activation barrier for shear-band arrest. An apparent energy barrier of ≈0.16 eV is found, i.e., the value derived in Section 4.2 for shear-band propagation of the same Zr-based (Vit105) MG is roughly twice the value of Q_{arr}. The earlier mentioned STZ theory shows that these two activation energies are related and should differ by a factor of 2–3,[20] which supports our view that there are many activation energy scales present in the deformation of MGs. It also shows that the energy scale derived from aging experiments (Figure 11d) can be related to STZ relaxation, while the corresponding apparent activation energy for shear-band propagation, Q_{prop}, cannot be ascribed to one specific mechanism.

Having motivated the assessment of shear-band arrest with the symmetric velocity profiles seen in Figure 8, the remaining task is to verify that the characteristic time scale t_c is indeed about half the value of Δt for shear-band propagation as obtained during serrated flow. This means, if t_c is representative for a thermally activated shear-band mechanism that governs about half the entire shear-band propagation cycle where $dv_{SB} / dt < 0$, then the characteristic time Δt for intermittent shear-band propagation is expected to follow the same temperature dependence as $2 \times t_c$. This is indeed the case, as was shown by plotting the logarithm of both time scales, Δt from the data in Figure 9 and $2 \times t_c$ from Figure 11d, as a function of T.[87] The resulting plot yields a consistent trend along one line with an overlap in the intermediate temperature regime (210–250 K).

The aging time analysis based on the data summarized in Figure 11 is empirical, but allows us to derive fundamental properties of shear-band dynamics in MGs. In fact, the observations made during our stress-aging experiments are representative for both multi-contact interfaces of a wide range of materials classes, including paper, sandstone, steels, and polymers, and also junction rheology of lubricated interfaces, well reflected in changes of the static friction coefficient as a function of waiting time.[61] This indicates a very generic and fundamental behavior for interfaces in contact, allowing us to conclude that the transition from a static to dynamic state (or inverse) is not described by a sudden unjamming-jamming (or jamming-unjamming) transition, but—and in agreement with the shear-band creep shown in Figure 11c—by a time and stress-dependent process. In the light of our shear-band initiation studies (Section 4.1), which infer the development of a softened layer being in a state equivalent to the undercooled liquid regime, the observed stress aging is of structural nature (but not interfacial). We note that structural aging has been shown to be sensitive to the applied tangential force[98] and is expected to depend on structural history. The latter issue was, however, not observed here, while the former could not be analyzed and may be inherently included in the data of Figure 11a. Nevertheless, nanoscale lubricated boundaries,[99] sheared glassy polymer interfaces,[97] and modeling efforts including STZs,[20,100] all reveal a consistent picture during stop-and-go shearing: upon arrest, that is, after the latency time t_c during which creep is observed, strengthening occurs via slow relaxation of the system to a stable configuration in the energy landscape that is characteristic of the quenched disorder; however, when motion sets in, higher energy states are repopulated (which were depopulated during aging). The derived energy scale of 0.16 eV for shear-band arrest is a value signifying the mean energy barrier for reaching a stable energetic configuration under an applied stress.

In the context of recent molecular dynamics (MD) simulations,[101,102] shear-band aging and arrest can be understood as a process during which broken bonds of specific atomic clusters (icosahedra and/or Kaspar polyhedra) reform. Those clusters have been shown to be structurally rigid compared to less ideally arranged motifs, and can during structural relaxation form a stiff interconnected network. Furthermore, MD simulations also reveal that such an interconnected network of icosahedra has a strongly enhanced formation rate at the glass transition during cooling.[103,104] Since the shear-band arrest process is effectively the reverse mechanism of a mechanically induced glass transition, one may assume that such atomistic processes are indeed at play when the shear-band material again freezes to become a solid. Subsequent aging that leads to increased mechanical stability (seen in the evolution of $\Delta\sigma$) is equally compatible with the observation that relaxation during MD simulations further strengthens the mechanical stability of the disordered structure. These questions will be further investigated in the future in the context of chemical influences on shear-band dynamics (see also the forthcoming study by Thurnheer et al.)[91]

4.4. Summarizing Stages and Time Scales in Shear-Band Dynamics

With the experimental insights presented in Sections 4.1 to 4.3 it is now possible to better understand the processes that occur within one stress-drop or displacement-jump cycle during serrated flow. **Figure 12** summarizes the different stages in a schematic manner. In the linear-elastic loading segment prior to the peak stress (Figure 4c) static aging occurs in the shear band, of which the amount is characterized by the stress-overshoot magnitude, $\Delta\sigma$.[87] Because static aging of a shear band was shown to be both time and temperature-dependent (Figure 11), this directly explains the decrease of the stress-drop (serration) magnitude with increasing strain rate. During the static-aging segment, $v_{SB} = 0$, and $du/dt \propto d\varepsilon_{appl}/dt$.

When a specific critical stress is reached, a shear band is formed via a shear-dilatation mechanism that has a time scale, Δt_{ini}, of some tens of μs at room temperature (Figure 6), and is accompanied with a median volume expansion of $\delta V/V_{SB} \approx$ 2%.[65] During this very short structural softening process, $v_{SB} = 0$ within the resolution of the experimental data, and $du/dt \propto d\varepsilon_{appl}/dt$. Subsequently, when being in the serrated flow-regime, $v_{SB} \propto du/dt >> d\varepsilon_{appl}/dt$, and a strong velocity gradient develops within the ≈20 nm thick shear band, under the assumption that the lower part of the sample does not translate laterally.

During shear-band propagation, v_{SB} follows a symmetric velocity profile (Figure 8) that does not show any steady-state flow. The acceleration, deceleration, and peak velocity are exponentially depending on temperature. At room temperature one full propagation process takes ≈1 ms (Δt_{prop}), and may take up to seconds at –80 °C.[80] Since a given testing temperature corresponds to one mean v_{SB}, it is clear that the increase of $d\varepsilon_{appl}/dt$ can directly suppress serrated flow at the critical point when $v_{SB} = K \times d\varepsilon_{appl}/dt$, where K is some factor converting the applied rate to a resolved shear rate (Figure 9). Passing this critical point yields non-serrated flow, and shear bands are driven at the applied rate. The fact that the velocity profile of one serration is symmetric reveals that half the propagation time is a deceleration process, suggesting that structural softening is reversed during deceleration. This regime was successfully probed during non-serrated flow, and is identified as shear-band creep that occurs during the second half of the velocity profile. We note that the terminology of creep originates from investigations during non-serrated flow at low temperatures, where the studied processes are slow and where $v_{SB} \propto du/dt > d\varepsilon_{appl}/dt = 0$. Nevertheless, the good agreement between the temperature dependence of creep time scales, and those derived from serrated flow motivates this conclusion. Shear-band creep times, Δt_{creep}, representing half the velocity profile, are consequently of the order of $0.5 \times \Delta t_{prop}$.[87] It is clear that this contains some degree of approximation, because the underlying atomistic relaxation process that first leads to a decrease in acceleration and subsequently to deceleration is assumed to set in at the inflection point where $d^2u/dt^2 = 0$ in the velocity profile. Shear-band creep is thus the stage during which the reverse process to initiation occurs (re-formation of structural units vs breaking of those). It can be described by the temperature-dependent latency time t_c (Figure 11), and is a part of the full propagation stage. Since the deceleration stage, as a part of the propagation stage, includes structural freezing, one may conclude that the majority of $\delta V/V_{SB}$ is recovered before reentering static aging. This is, however, not the case, given the compelling evidence from recent TEM studies that reveal a residual dilatation of the same spread and magnitude as obtained during in situ AE testing (Figure 7).[75]

Subsequent to creep, or the structural freezing process in the shear band, arrest sets in.[87] Now $v_{SB} \rightarrow 0$, and static aging is again at play during the following phase where $du/dt \propto d\varepsilon_{appl}/dt$. Despite creep and arrest being part of shear-band propagation, they are both located in a dashed box in Figure 12, because they were derived under conditions where the external drive was set to 0.

5. Unsolved Questions and Future Directions

With the large amount of literature on post-mortem analysis of shear bands in MGs, and with the recent progress made in-real time probing of shear-band operations, structural and dynamic mechanisms of shear banding can now be understood more quantitatively. The measurements summarized in this report also show that with simple experimental means one can gain fundamental insights into local and relatively fast dynamic

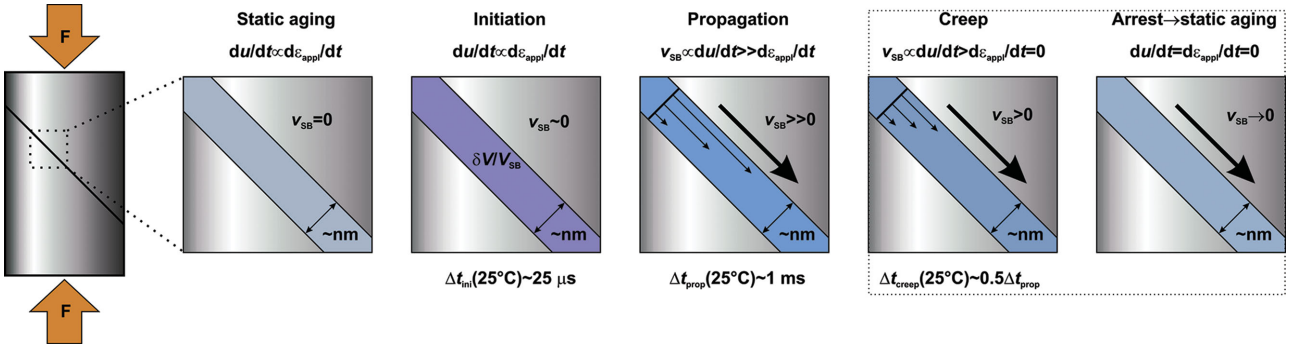

Figure 12. Schematic representation of the different shear-banding stages discussed in this work. Since shear-band creep and arrest are part of shear-band propagation, they are both contained within a dashed box. The characteristic time scales for shear-band initiation, shear-band propagation and shear-band creep, which finally leads to shear-band arrest, are indicated in the figure.

processes. With the knowledge of the different dynamic stages of shear banding in MGs, dedicated questions to each stage should be the focus of future investigations, some of which are the following: i) Is shear-band initiation a percolative process or a propagation front mechanism? ii) The high local shear rates within the presumably nm-thick shear band drive the system far from equilibrium, but why do simple equilibrium viscosity approaches work seemingly well? iii) How are the derived activation barriers for both shear-band propagation and shear-band arrest linked to the underlying structural state? iv) Would there potentially be a correlation between the various activation energies and the topological and chemical disorder of the matrix, or even macroscopic quantities such as for example T_g? v) How can we quantitatively extract a stress and plastic strain dependence from both the shear-band velocity and the characteristic relaxation time that determines shear-band arrest? Most of these questions are directly related to the structure evolution within a shear band, which requires time-resolved structural probing at the nanometer scale. We believe that the rapid development of high-speed characterization techniques will soon allow us to answer these questions, and to teach us how to ultimately tune the parameters that dictate the dynamics of shear-banding—the key to prevent rapid run-away failure of metallic glasses. In the meantime the progress made with MD simulations and STZ modeling will serve us as a guidance for new specific experiments to unravel atomic-scale structural processes in shear-band dynamics.

Acknowledgements

The authors thank D. Klaumünzer, P. Thurnheer, P. M. Derlet, G. Villard, and E. Preiß for their contributions to the different aspects of this research. J.F.L. is grateful for the continuous financial support by the Swiss National Science Foundation (SNF No. 200020–120258, SNF No. 200020–135100, and SNF No. 200020–153103). R.M. thanks the Alexander von Humboldt Foundation for financial support and C.A. Volkert for institutional support at the University of Göttingen.

Received: November 28, 2014
Revised: February 12, 2015
Published online: March 18, 2015

[1] N. Hu, J. F. Molinari, *J. Mech. Phys. Solids* **2004**, *52*, 499.
[2] Q. Wei, D. Jia, K. T. Ramesh, E. Ma, *Appl. Phys. Lett.* **2002**, *81*, 1240.
[3] P. D. Olmsted, *Rheol. Acta* **2008**, *47*, 283.
[4] R. N. Haward, R. J. Young, *The Physics of Glassy Polymers*, Chapman & Hall, London **1997**.
[5] C. A. Schuh, T. C. Hufnagel, U. Ramamurty, *Acta Mater.* **2007**, *55*, 4067.
[6] M. M. Trexler, N. N. Thadhani, *Prog. Mater. Sci.* **2010**, *55*, 759.
[7] W. H. Wang, C. Dong, C. H. Shek, *Mater. Sci. Eng. R-Rep.* **2004**, *44*, 45.
[8] J. F. Löffler, *Intermetallics* **2003**, *11*, 529.
[9] F. Spaepen, *Acta Metallurgica* **1977**, *25*, 407.
[10] D. Turnbull, M. H. Cohen, *J. Chem. Phys.* **1961**, *34*, 120.
[11] A. S. Argon, *Acta Metall.* **1979**, *27*, 47.
[12] A. S. Argon, H. Y. Kuo, *Mater. Sci. Eng.* **1979**, *39*, 101.
[13] M. L. Falk, J. S. Langer, *Phys. Rev. E* **1998**, *57*, 7192.
[14] J. S. Langer, M. L. Manning, *Phys. Rev. E* **2007**, *76*, 056107.
[15] M. L. Falk, J. S. Langer, *Annu. Rev. Condens. Matter Phys.* **2011**, *2*, 353.
[16] M. L. Manning, J. S. Langer, J. M. Carlson, *Phys. Rev. E* **2007**, *76*, 056106.
[17] M. L. Manning, E. G. Daub, J. S. Langer, J. M. Carlson, *Phys. Rev. E* **2009**, *79*, 016110.
[18] C. H. Rycroft, F. Gibou, *J. Comput. Phys.* **2012**, *231*, 2155.
[19] E. Bouchbinder, J. S. Langer, I. Procaccia, *Phys. Rev. E* **2007**, *75*, 036107.
[20] E. G. Daub, D. Klaumunzer, J. F. Löffler, *Phys. Rev. E* **2014**, *90*, 062405.
[21] P. M. Derlet, R. Maass, *Philos. Mag.* **2014**, *94*, 2776.
[22] P. M. Derlet, R. Maass, *Philos. Mag.* **2013**, *93*, 4232.
[23] P. M. Derlet, R. Maass, *Phys. Rev. B* **2012**, *84*, 220201.
[24] G. T. Barkema, N. Mousseau, *Phys. Rev. Lett.* **1996**, *77*, 4358.
[25] D. Rodney, C. A. Schuh, *Phys. Rev. B* **2009**, *80*, 184203.
[26] D. Rodney, C. Schuh, *Phys. Rev. Lett.* **2009**, *102*.
[27] S. Swayamjyoti, J. F. Löffler, P. M. Derlet, *Phys. Rev. B* **2014**, *89*, 224201.
[28] Y. Fan, T. Iwashita, T. Egami, *Nat. Commun.* **2014**, *5*, 5083.
[29] J. Lu, G. Ravichandran, W. L. Johnson, *Acta Mater.* **2003**, *51*, 3429.
[30] W. L. Johnson, K. Samwer, *Phys. Rev. Lett.* **2005**, *95*, 195501.
[31] P. E. Donovan, *Acta Metall.* **1989**, *37*, 445.
[32] A. S. Bakai, S. A. Bakai, I. M. Mikhailovskii, I. M. Neklyudov, P. I. Stoev, M. P. Macht, *Jetp Lett.* **2002**, *76*, 218.
[33] W. F. Wu, Y. Li, C. A. Schuh, *Philos. Mag.* **2008**, *88*, 71.
[34] Granta Design – Material Intelligence, CES Selector Database.
[35] L. Tian, Y.-Q. Cheng, Z.-W. Shan, J. Li, C.-C. Wang, X.-D. Han, J. Sun, E. Ma, *Nat. Commun.* **2012**, *3*.
[36] K. Mondal, K. Hono, *Mater. Trans.* **2009**, *50*, 152.
[37] R. Maass, D. Klaumünzer, E. I. Preiss, P. M. Derlet, J. F. Löffler, *Scr. Mater.* **2012**, *66*, 231.
[38] H. J. Leamy, H. S. Chen, T. T. Wang, *Metall. Trans.* **1972**, *3*, 699.
[39] Y. Zhang, N. A. Stelmashenko, Z. H. Barber, W. H. Wang, J. J. Lewandowski, A. L. Greer, *J. Mater. Res.* **2007**, *22*, 419.
[40] W. J. Wright, R. B. Schwarz, W. D. Nix, *Mater. Sci. Eng. A* **2001**, *319*, 229.
[41] F. H. Dalla Torre, A. Dubach, J. Schällibaum, J. F. Löffler, *Acta Mater.* **2008**, *56*, 4635.
[42] A. R. Yavari, A. Le Moulec, A. Inoue, N. Nishiyama, N. Lupu, E. Matsubara, W. J. Botta, G. Vaughan, M. Di Michiel, A. Kvick, *Acta Mater.* **2005**, *53*, 1611.
[43] K. M. Flores, B. P. Kanungo, S. C. Glade, P. Asoka-Kumar, *J. Non-Cryst. Solids* **2007**, *353*, 1201.
[44] W. Dmowski, Y. Yokoyama, A. Chuang, Y. Ren, M. Umemoto, K. Tsuchiya, A. Inoue, T. Egami, *Acta Mater.* **2010**, *58*, 429.
[45] P. E. Donovan, W. M. Stobbs, *Acta Metall.* **1981**, *29*, 1419.
[46] Y. Zhang, A. L. Greer, *Appl. Phys. Lett.* **2006**, *89*, 071907.
[47] J. Li, Z. L. Wang, T. C. Hufnagel, *Phys. Rev. B* **2002**, *65*.
[48] S. Pauly, M. H. Lee, D. H. Kim, K. B. Kim, D. J. Sordelet, J. Eckert, *J. Appl. Phys.* **2009**, *106*, 103518.
[49] A. C. Y. Liu, D. M. Paganin, L. Bourgeois, P. N. H. Nakashima, R. T. Ott, M. J. Kramer, *Phys. Rev. B* **2011**, *84*, 7.
[50] G. Wilde, H. Rösner, *Appl. Phys. Lett.* **2011**, *98*, 251904.
[51] J. Bokeloh, S. V. Divinski, G. Reglitz, G. Wilde, *Phys. Rev. Lett.* **2011**, *107*, 235503.
[52] J. Pan, Q. Chen, L. Liu, Y. Li, *Acta Mater.* **2011**, *59*, 5146.
[53] R. Maass, K. Samwer, W. Arnold, C. A. Volkert, *Appl. Phys. Lett.* **2014**, *105*, 171902.
[54] P. F. Guan, M. W. Chen, T. Egami, *Phys. Rev. Lett.* **2010**, *104*, 205701.
[55] A. L. Greer, Y. Q. Cheng, E. Ma, *Mater. Sci. Eng. R-Rep.* **2013**, *74*, 71.

[56] W. J. Wright, M. W. Samale, T. C. Hufnagel, M. M. LeBlanc, J. N. Florando, *Acta Mater.* **2009**, *57*, 4639.
[57] H. Kimura, T. Masumoto, *Acta Metall.* **1983**, *31*, 231.
[58] H. Kimura, T. Masumoto, *Philos. Mag. A-Phys. Condens. Matter Struct. Defect Mech. Prop.* **1981**, *44*, 1021.
[59] H. Kimura, T. Masumoto, *Philos. Mag. A-Phys. Condens. Matter Struct. Defect Mech. Prop.* **1981**, *44*, 1005.
[60] D. Klaumünzer, R. Maass, J. F. Löffler, *J. Mater. Res.* **2011**, *26*, 1453.
[61] T. Baumberger, C. Caroli, *Adv. Phys.* **2006**, *55*, 279.
[62] A. Dubach, F. H. Dalla Torre, J. F. Löffler, *Philos. Mag. Lett.* **2007**, *87*, 695.
[63] A. Dubach, F. H. Dalla Torre, J. F. Löffler, *Acta Mater.* **2009**, *57*, 881.
[64] S. Nasuno, A. Kudrolli, A. Bak, J. P. Gollub, *Phys. Rev. E* **1998**, *58*, 2161.
[65] D. Klaumünzer, A. Lazarev, R. Maass, F. H. Dalla Torre, A. Vinogradov, J. F. Löffler, *Phys. Rev. Lett.* **2011**, *107*, 185502.
[66] F. H. Dalla Torre, D. Klaumünzer, R. Maass, J. F. Löffler, *Acta Mater.* **2010**, *58*, 3742.
[67] A. Vinogradov, *Scr. Mater.* **2010**, *63*, 89.
[68] A. Vinogradov, A. Danyuk, V. A. Khonik, *J. Appl. Phys.* **2013**, *113*.
[69] C. B. Scruby, G. R. Baldwin, K. A. Stacey, *Int. J. Fract.* **1985**, *28*, 201.
[70] J. Megusar, A. S. Argon, N. J. Grant, *Mater. Sci. Eng.* **1979**, *38*, 63.
[71] A. S. Argon, J. Megusar, N. J. Grant, *Scr. Metall.* **1985**, *19*, 591.
[72] R. W. Cahn, N. A. Pratten, M. G. Scott, H. R. Sinning, L. Leonardsson, *Mat. Res. Soc. Symp. Proc.* **1984**, *28*, 241.
[73] C. A. Pampillo, H. S. Chen, *Mater. Sci. Eng.* **1974**, *13*, 181.
[74] M. H. Cohen, D. Turnbull, *J. Chem. Phys.* **1959**, *31*, 1164.
[75] H. Rösner, M. Peterlechner, C. Kuebel, V. Schmidt, G. Wilde, *Ultramicroscopy* **2014**, *142*, 1.
[76] S. Ogata, F. Shimizu, J. Li, M. Wakeda, Y. Shibutani, *Intermetallics* **2006**, *14*, 1033.
[77] F. Shimizu, S. Ogata, J. Li, *Acta Mater.* **2006**, *54*, 4293.
[78] E. R. Homer, *Acta Mater.* **2014**, *63*, 44.
[79] Y. Q. Cheng, Z. Han, Y. Li, E. Ma, *Phys. Rev. B* **2009**, *80*, 134115.
[80] R. Maass, D. Klaumünzer, J. F. Löffler, *Acta Mater.* **2011**, *59*, 3205.
[81] S. X. Song, X. L. Wang, T. G. Nieh, *Scr. Mater.* **2010**, *62*, 847.
[82] W. J. Wright, R. R. Byer, X. Gu, *Appl. Phys. Lett.* **2013**, *102*.
[83] D. Klaumünzer, R. Maass, F. H. D. Torre, J. F. Löffler, *Appl. Phys. Lett.* **2010**, *96*, 061901.
[84] P. Thurnheer, R. Maass, S. Pogatscher, J. F. Löffler, *Appl. Phys. Lett.* **2014**, *104*, 101910.
[85] S. X. Song, T. G. Nieh, *Intermetallics* **2009**, *17*, 762.
[86] Z. Han, W. F. Wu, Y. Li, Y. J. Wei, H. J. Gao, *Acta Mater.* **2009**, *57*, 1367.
[87] R. Maass, D. Klaumünzer, G. Villard, P. M. Derlet, J. F. Löffler, *Appl. Phys. Lett.* **2012**, *100*, 071904.
[88] E. J. Kramer, *J. Polym. Sci. B, Polym. Phys.* **1975**, *13*, 509.
[89] W. H. Wang, *J. Appl. Phys.* **2011**, *110*.
[90] P. Koziatek, J.-L. Barrat, P. Derlet, D. Rodney, *Phys. Rev. B* **2013**, *87*.
[91] P. Thurnheer, R. Maass, K. Laws, S. Pogatscher, J. F. Löffler, unpublished.
[92] C. A. Schuh, A. C. Lund, T. G. Nieh, *Acta Mater.* **2004**, *52*, 5879.
[93] A. Kawashima, Y. Zeng, M. Fukuhara, H. Kurishita, N. Nishiyama, H. Miki, A. Inoue, *Mater. Sci. Eng. A* **2008**, *498*, 475.
[94] H. Q. Li, C. Fan, K. X. Tao, H. Choo, P. K. Liaw, *Adv. Mater.* **2006**, *18*, 752.
[95] B. Yang, P. K. Liaw, G. Wang, M. Morrison, C. T. Liu, R. A. Buchanan, Y. Yokoyama, *Intermetallics* **2004**, *12*, 1265.
[96] J. J. Lewandowski, A. L. Greer, *Nat. Mater.* **2006**, *5*, 15.
[97] P. Berthoud, T. Baumberger, C. G'Sell, J. M. Hiver, *Phys. Rev. B* **1999**, *59*, 14313.
[98] L. Bureau, T. Baumberger, C. Caroli, *Eur. Phys. J. E* **2002**, *8*, 331.
[99] S. Yamada, *Langmuir* **2008**, *24*, 1469.
[100] A. Lemaitre, J. Carlson, *Phys. Rev. E* **2004**, *69*, 061611.
[101] A. J. Cao, Y. Q. Cheng, E. Ma, *Acta Mater.* **2009**, *57*, 5146.
[102] J. Ding, Y.-Q. Cheng, E. Ma, *Acta Mater.* **2014**, *69*, 343.
[103] R. E. Baumer, M. J. Demkowicz, *Phys. Rev. Lett.* **2013**, *110*, 145502.
[104] J. Zemp, M. Celino, B. Schönfeld, J. F. Löffler, *Phys. Rev. B* **2014**, *90*, 144108.